International Journal of Nanomedicine

Dovepress
open access to scientific and medical research

Open Access Full Text Article

ORIGINAL RESEARCH

Molecular Imaging of Inflammation in a Mouse Model of Atherosclerosis Using a Zirconium-89-Labeled Probe

This article was published in the following Dove Press journal:
International Journal of Nanomedicine

Mona Ahmed[1,2]
Tetyana Tegnebratt[3,4]
Thuy A Tran[3,4]
Li Lu[3,4]
Peter Damberg[3]
Anton Gisterå[5]
Laura Tarnawski[5]
Dianna Bone[1,6]
Ulf Hedin[1,7]
Per Eriksson[5]
Staffan Holmin[3,8]
Björn Gustafsson[1,*]
Kenneth Caidahl[1,6,9,10,*]

[1]Department of Molecular Medicine and Surgery, Center for Molecular Medicine, BioClinicum, Karolinska Institutet, Stockholm, SE 17176, Sweden; [2]Department of Cardiology, Karolinska University Hospital, Stockholm, SE 17176, Sweden; [3]Department of Clinical Neuroscience, BioClinicum, Karolinska Institutet, Stockholm, SE 17176, Sweden; [4]Department of Radiopharmacy, Karolinska University Hospital, Stockholm, SE 17176, Sweden; [5]Department of Medicine Solna, Center for Molecular Medicine, BioClinicum, Karolinska Institutet, Stockholm, SE 17176, Sweden; [6]Department of Clinical Physiology, Karolinska University Hospital, Stockholm, SE 17176, Sweden; [7]Department of Vascular Surgery, Karolinska University Hospital, Stockholm, SE 17176, Sweden; [8]Department of Neuroradiology, Karolinska University Hospital, Stockholm, SE 17176, Sweden; [9]Department of Clinical Physiology, Region Västra Götaland, Sahlgrenska University Hospital, Gothenburg, SE 41345, Sweden; [10]Department of Molecular and Clinical Medicine, Institute of Medicine, Sahlgrenska Academy, University of Gothenburg, Gothenburg, SE 41345, Sweden

*These authors contributed equally to this work.

Correspondence: Mona Ahmed
Email mona.ahmed@ki.se

Background: Beyond clinical atherosclerosis imaging of vessel stenosis and plaque morphology, early detection of inflamed atherosclerotic lesions by molecular imaging could improve risk assessment and clinical management in high-risk patients. To identify inflamed atherosclerotic lesions by molecular imaging in vivo, we studied the specificity of our radiotracer based on maleylated (Mal) human serum albumin (HSA), which targets key features of unstable atherosclerotic lesions.

Materials and Methods: Mal-HSA was radiolabeled with a positron-emitting metal ion, zirconium-89 ($^{89}Zr^{4+}$). The targeting potential of this probe was compared with unspecific ^{89}Zr-HSA and ^{18}F-FDG in an experimental model of atherosclerosis (*Apoe*$^{-/-}$ mice, n=22), and compared with wild-type (WT) mice (C57BL/6J, n=21) as controls.

Results: PET/MRI, gamma counter measurements, and autoradiography showed the accumulation of ^{89}Zr-Mal-HSA in the atherosclerotic lesions of *Apoe*$^{-/-}$ mice. The maximum standardized uptake values (SUV_{max}) for ^{89}Zr-Mal-HSA at 16 and 20 weeks were 26% and 20% higher ($P<0.05$) in *Apoe*$^{-/-}$ mice than in control WT mice, whereas no difference in SUV_{max} was observed for ^{18}F-FDG in the same animals. ^{89}Zr-Mal-HSA uptake in the aorta, as evaluated by a gamma counter 48 h postinjection, was 32% higher ($P<0.01$) for *Apoe*$^{-/-}$ mice than in WT mice, and the aorta-to-blood ratio was 8-fold higher ($P<0.001$) for ^{89}Zr-Mal-HSA compared with unspecific ^{89}Zr-HSA. HSA-based probes were mainly distributed to the liver, spleen, kidneys, bone, and lymph nodes. The phosphor imaging autoradiography (PI-ARG) results corroborated the PET and gamma counter measurements, showing higher accumulation of ^{89}Zr-Mal-HSA in the aortas of *Apoe*$^{-/-}$ mice than in WT mice (9.4±1.4 vs 0.8±0.3%; $P<0.001$).

Conclusion: ^{89}Zr radiolabeling of Mal-HSA probes resulted in detectable activity in atherosclerotic lesions in aortas of *Apoe*$^{-/-}$ mice, as demonstrated by quantitative in vivo PET/MRI. ^{89}Zr-Mal-HSA appears to be a promising diagnostic tool for the early identification of macrophage-rich areas of inflammation in atherosclerosis.

Keywords: positron emission tomography, molecular imaging, zirconium, human serum albumin, atherosclerosis, macrophages

Introduction

Atherosclerosis is a chronic inflammatory disease of the arterial wall that develops slowly over the decades. The disease has severe consequences for both society and individuals, and is a leading risk factor for cardiovascular disease, including myocardial infarction and stroke.[1]

Current clinical diagnostic tools are based on nontargeted visualization of the vasculature, such as angiography, or computed tomography (CT) and magnetic

resonance (MR) angiography with blood contrast.[2] Visualization of the vascular layers with invasive imaging techniques may enable the measurement of cap thickness and thus help direct the intervention,[2] but these techniques are invasive and associated with certain risks. The backbone of imaging is based on the degree of luminal stenosis or calcium score to identify treatable lesions. However, plaques that are vulnerable to rupture or at risk of plaque erosion can exist without impingement of the lumen. In the case of nonsignificant luminal stenosis, currently available clinical methods fail to predict accurately the progressive changes within the plaque that precede symptomatic plaque disruption. Numerous studies have shown that high macrophage content, especially in the plaque shoulder region, correlates with plaque vulnerability.[1,3] Hence, the degree of inflammation might better predict plaques that are prone to rupture.[1,4]

The search for methods to identify these vulnerable plaques has attracted considerable interest and includes the use of several imaging modalities,[2,5] such as ultrasound,[6–8] MR imaging (MRI),[9,10] and positron emission tomography (PET),[11,12] as well as combinations of the latter two methods.[13] The most common clinical radiotracer in PET imaging involves the use of ^{18}F radiolabeled fluorodeoxyglucose (^{18}F-FDG).[14] Increasingly, the benefits that come with PET molecular imaging have also been explored for identifying vascular inflammation.[11,12,14-17] However, because the inflammatory component of atherosclerotic plaques is usually not very prominent or visible with available clinical imaging applications or contrast agents, more specific PET tracers than FDG are being sought.[13,16,18-22] Amongst the newly developed and most promising radiotracers targeting vulnerable plaque features, some have recently been tested in human subjects, eg ^{18}F-sodium fluoride (^{18}F-NaF)[23] and gallium-68-labeled DOTATATE (^{68}Ga-DOTATATE).[24]

Molecular imaging tools could provide quantitative information utilizing specific and targeted molecular probes for detailed information on a cellular and molecular level, and thus improve the accuracy in identifying patients at risk of plaque rupture.

We recently suggested the use of such a tracer, zirconium-89-labeled maleylated human serum albumin (^{89}Zr-Mal-HSA), which specifically targets the macrophage scavenger receptor SR-A1.[25] This receptor is an attractive target for diagnostic purposes as it is expressed on macrophages in the cap area, and inside the atherosclerotic lesion of human plaques,[26,27] but not by vascular smooth muscle cells (vSMCs) and endothelial cells lining normal vasculature in non-plaque areas.[28,29] SR-A1 exacerbates atherogenesis by promoting macrophage development into foam cells and stimulating the secretion of proinflammatory cytokines.[28,30] In the present study, we evaluated ^{89}Zr-labeled tracers in a mouse model of atherosclerosis and compared them with ^{18}F-FDG. Our radiotracer enabled quantitative molecular imaging of inflamed atherosclerotic lesions by PET/MRI and enables early detection of inflamed atherosclerotic lesions.

Materials and Methods

Preparation of Radiotracers and FITC-Labeled Probes

The synthesis and characterization of the probes were previously reported by Ahmed et al.[25] In brief, *Para*-isothiocyanatobenzyl-deferoxamine (*p*-NCS-Bz-DFO; CheMatech, Dijon, France) or fluorescein isothiocyanate (FITC; Sigma-Aldrich, St. Louis, MO, USA) were conjugated to human serum albumin (HSA; Sigma-Aldrich) by adding p-NCS-Bz-DFO or FITC to HSA and stirring at room temperature (RT) and stable pH. The products were purified on a desalting column, and the product was freeze-dried. To conjugate the maleic anhydride (MalA), solid MalA was added while stirring at RT to a solution of HSA-DFO or HSA-FITC at pH 9. The resulting Mal-HSA -DFO was purified by dialysis and the Mal-HSA-FITC was purified on a desalting column. Solutions of the products were sterile filtered and freeze-dried. The approximate average numbers of conjugated FITC, DFO, and Mal groups could be determined by comparisons of the average molecular masses of the different HSA modifications with the molecular mass of unconjugated HSA. The respective masses were analyzed by mass spectrometry (MS) (Bruker ultrafleXtreme MALDI-TOF/TOF with a Smartbeam-II laser (Bruker Daltonik, Bremen, Germany)).

Radiolabeling and Quality Control

The radiolabeling of HSA was performed according to a method previously described by Ahmed et al.[25] In brief, 0.3 mg (1 mg/mL in 0.5 M HEPES buffer, Thermo Fisher Scientific, Waltham, MA, USA) of R-HSA-DFO (R = Mal or nonmodified) was added to a neutralized solution of ^{89}Zr; ~80–100 MBq ^{89}Zr(IV) oxalate ($t_{½}$ (^{89}Zr) = 78.4 h) in 1 M oxalic acid (PerkinElmer, BV Cyclotron VU, Amsterdam, The Netherlands); the pH was adjusted to 7–7.2 with 1 M sodium carbonate. The reaction was then

continued for 1 h on a Thermo Shaker set to 21°C and 450 rpm.

To analyze and purify the radiolabeled tracers (^{89}Zr-Mal-HSA and ^{89}Zr-HSA), high-performance liquid chromatography (HPLC; LC-10AD VP, Shimadzu, Kyoto, Japan with a Superdex 75 10/300 GL column, 0.5 mL/min 1× phosphate buffered saline (PBS), 210 nm) equipped with a radiodetector (Model 170 Radioisotope Detector, Beckman Instruments, Pasadena, CA, USA), was used and the radiolabeled tracers were collected in 16–20 small fractions. The subfractions used for imaging were taken from the highest ~30% of the radio peak. The labeling yield and radiochemical purity of the ^{89}Zr-labeled tracers (^{89}Zr-Mal-HSA and ^{89}Zr-HSA) were determined by instant thin-layer chromatography (iTLC), eluted with 0.2 M citric acid (Sigma-Aldrich). The radioactive biodistribution in the iTLC strip was quantified on a TLC-scanner (Biodex Medical Systems, Shirley, NY, USA) using Winscan software (Biodex Medical Systems).

Mice

As a disease model, female apolipoprotein E null mice (*Apoe*$^{-/-}$) (Jackson Laboratories) were used (n=22). The *Apoe*^{tm1Unc} mutant strain was developed in the laboratory of Dr. Nobuyo Maeda at the University of North Carolina at Chapel Hill. Female C57BL/6J wild-type (WT) mice (Jackson Laboratories) were used as control animals (n=21). The C57BL/6J strain was produced by backcrossing the *Apoe*^{tm1Unc} mutation 10 times to C57BL/6J mice. All animals were age and diet matched for all experiments. To accelerate plaque progression, the animals were fed a Western diet (WD) (21% fat, 0.15% cholesterol, R638 Lantmännen Lantbruk, Specialdieter; Kimstad, Sweden) from 8 weeks of age until 20 weeks of age. An additional group of female WD-fed *Apoe*$^{-/-}$ mice (n=27, 20 weeks of age) were used for a biodistribution study.

Imaging Protocol

For the imaging experiments, the mice were anesthetized using an isoflurane/oxygen gas mixture (4% for induction, 1.5–2% for maintenance). The anesthetic concentration was regulated using an E-Z Anesthesia Vaporizer and blended with 7:3 air/O_2 (Euthanex Corporation, PA, USA). Core body temperature was controlled and maintained at 37°C using a rectal thermistor probe and feedback-controlled homeothermic heating pad during anesthesia. For imaging, mice were placed in custom-made 3D-printed beds to standardize the positioning of the mice during scanning and facilitate the overlay of images from MR and microPET imaging from the same mouse. Each mouse was scanned by PET at ages 16 and 20 weeks and by MRI once at an average age of 17.3±1.5 weeks. Immediately after the 48 h time point on the second imaging week, each mouse was euthanized (using 5% isoflurane) for ex vivo analyses. The overall study plan is shown in Figure 1.

MicroPET Imaging

The imaging procedure consisted of PET imaging using ^{18}F-FDG (~7 MBq/animal) on day 1 (30 min static scan, 40–60 min postinjection [p.i.]); ^{89}Zr-HSA or ^{89}Zr-Mal-HSA radiotracers (~5 MBq/animal) on day 2 (1 h dynamic scan and 30 min static scan, 4 h p.i.), day 3 (30 min static scan, 24 h p.i.), and day 4 (30 min static scan, 48 h p.i.). A detailed protocol for the PET imaging is described elsewhere.[31] Briefly, for each PET imaging session, two animals were scanned simultaneously: an *Apoe*$^{-/-}$ and WT mouse. ^{18}F-FDG (t½ = 109.8 min) for clinical use was produced on site (Dept. of Radiopharmacy, Karolinska University Hospital), following all the requirements for human use and was used without further purification. Dilution with sterile 0.9% saline was carried out as necessary. Each animal received an injection of ~100–200 µL (max. 10 mL/kg body weight) of the radiotracer diluted in 0.9% saline and a radioactive dose.

The ^{18}F-FDG PET (n=43; 22 *Apoe*$^{-/-}$ and 21 WT mice), ^{89}Zr-Mal-HSA PET (n=23; 12 *Apoe*$^{-/-}$ and 11 WT mice), and control radiotracer ^{89}Zr-HSA PET (n=20; 10 *Apoe*$^{-/-}$ and 10 WT mice) scans were performed using the MicroPET Focus 120 scanner (CTI-Concorde Microsystems, Knoxville, TN, USA). PET data were acquired in the 3D mode, and the images were reconstructed by standard 2D filtered back projection using a ramp filter. PET data were processed using the MicroPET Manager and evaluated using the Inveon Research Workplace (IRW) software (Siemens Medical Systems, Malvern, PA, USA). To quantify the radioactivity accumulation of the ^{18}F-FDG and the ^{89}Zr-labeled tracers in the aortic arch of the animals, the images from PET and MRI scans were first coregistered in the IRW software; then, volumes of interest (VOIs) were manually drawn around the aortic arch (100–160 mm^3) on the MR image for the measurements of intensities as the maximum standardized uptake value (SUV_{max}) from the radiolabeled compound on the PET image. The activity (SUV_{mean}) originating from the blood pool was measured in a VOI (4.8 mm^3) drawn in the inferior vena cava (located 30 mm

below the top of the aortic arch VOI) on the PET image using the earliest time points (0–20 s p.i.) to identify the vessel. Quantification of the ^{18}F-FDG uptake was performed on PET images acquired 40–60 min p.i., and the mean SUV_{max} values in the aortic arch VOIs were measured throughout the whole 30-min static scan. To quantify the uptake of the ^{89}Zr-labeled tracers, the mean SUV_{max} value in each VOI from the last 15 min (when the activities had stabilized, ie, 45 min p.i.) of the 1 h dynamic scans was used. The radioactivity was quantified and presented using standardized uptake values (calculated as voxel intensity [MBq]/VOI volume [mL])/(injected activity [MBq]/animal body weight [g]), and target-to-background ratios (TBRs) for aortic arch and blood pool. TBRs were calculated as follows: TBR = (plaque activity)/(blood pool activity). Additionally, the time–radioactivity curves (TRCs) for the ^{89}Zr-labeled tracers and for the pure ^{89}Zr radioisotope were obtained for the first-hour p.i.

Magnetic Resonance Imaging

Each mouse was imaged by MRI once. MRI was performed at 9.4 T using a scanner with a horizontal bore (Varian, Yarnton, UK) and equipped with a millipede coil with an inner diameter of 30 mm and a gradient insert with an inner diameter of 12 cm. The mouse was anesthetized and placed in a prone position on a 3D-printed animal bed that was identical to the beds used for PET scanning. Subcutaneous needle electrodes were positioned in the right forelimb and left hind limb for electrocardiography (ECG) (SA Instruments, Stony Brook, NY, USA). A respiration pillow was fixed to the bed under the abdomen, and the core body temperature was measured by a rectal thermistor probe and maintained at 37°C through a feedback-controlled warm air system (SA Instruments).

Bright blood MR images, enabling the delineation of relevant regions of interest (ROIs), were acquired with prospective triggering to the ECG with one excitation per expiration period. Therefore, the repetition time (TR) was determined by the respiration rate, which was in the range of 40–100 breaths per minute. The scanning parameters were echo time (TE), 2.76 ms, flip angle, 90°, field-of-view (FOV) 10.24 × 25.6 mm^2 (or 10.24 × 38.4 mm^2 if needed to avoid aliasing), matrix size 512×128 (or 512 × 192 for larger FOV), and slice thickness 0.4 mm. The read and phase encode directions were in the plane of the aortic arch, and the experiment was repeated with incremented slice positions to cover the heart.

To facilitate coregistration with the PET images, a complementary data set covering the entire chest of the animal with 64 slices was also acquired. The slices were registered with the bright blood image but acquired with a multislice loop, where data from eight slices were acquired following each ECG trigger within the allowed expiration phase. Scanning parameters were TE, 3.24 ms, flip angle, 70°, FOV 10.24 × 25.6 mm^2 (or 10.24 × 38.4 mm^2 if needed to avoid phase wraparound), and matrix size 512 × 128 (or 512 × 192 for the larger FOV).

Corresponding slices in the stack were replaced by bright blood images before manual coregistration with the PET data. In a few cases, minor operator errors in the slice planning motivated spline interpolation to correctly merge the data sets, which did not impede delineation of the relevant regions or coregistration with the PET data.

Black blood (spin-echo with a TE of 9.56 ms) and bright blood (gradient echo with a TE of 1.85 ms and flip angle of 90°) from a cross-sectional 0.6 mm slice through the root of the aorta were also acquired (matrix size 256 × 256 and FOV 25.6 × 25.6 mm^2). Both sequences were triggered by the ECG within the expiration period, making the TR equal to the respiration period.

Blocking Study

To illustrate the effects of presaturation of the liver and spleen uptake capacity for Mal-HSA, we evaluated six mice in a blocking study. An intravenous dose of 1 mg nonradiolabeled Mal-HSA was injected in *Apoe*$^{-/-}$ mice (n=3) and circulated for 15 min prior to injection of ^{89}Zr-Mal-HSA. Three additional *Apoe*$^{-/-}$ mice were injected with only radiolabeled probe and used as controls. The mice were anesthetized according to the imaging protocol, sacrificed 1 h p.i. and dissected for gamma counter measurement of the radioactive signal in the aorta, blood, heart, liver, and spleen.

Biodistribution

To assess the blood clearance dynamics of the agents and sites of their accumulation over time, biodistribution studies of ^{89}Zr-HSA and ^{89}Zr-Mal-HSA were performed. ^{89}Zr-labeled HSA and Mal-HSA were injected into the tail vein and the animals were euthanized at 1, 4, 24, and 48 h p.i. At each time point, organs were dissected, placed in scintillation vials, weighed, and radioactivity was measured in a gamma counter (Wallac Wizard 3" 1480, PerkinElmer, Waltham, MA, USA). To compare with the HSA-based probes, the biodistribution of ^{18}F-FDG in mice was evaluated in a pilot study (n=4). Data were calculated

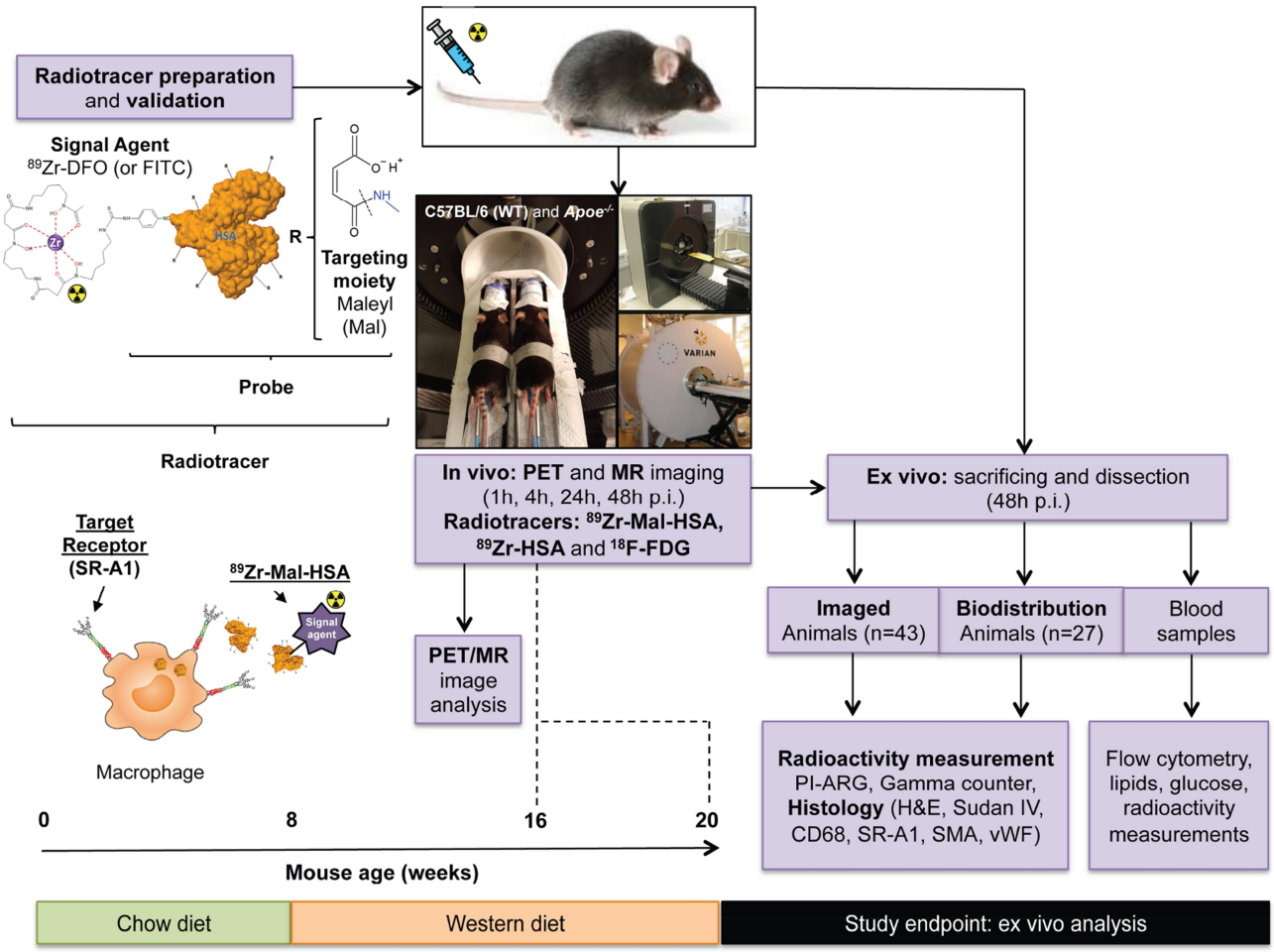

Figure 1 The overall study design. Starting with radiotracer preparation and quality controls; a schematic is shown of the radiotracer with the ^{89}Zr-labeled HSA modification followed by animal preparation, in vivo imaging, and ex vivo measurements and analyses. A timeline of the study is provided, showing the diet throughout the course of the study.

as the percentage of injected dose per g of tissue (%ID/g). A description of ex vivo tissue- and blood analysis is given in the Electronic Supplementary Material.

Phosphor Imaging Autoradiography

For digital Phosphor Imaging Autoradiography (PI-ARG) of atherosclerosis, frozen 8 µm sections of mouse aortic roots were mounted on glass slides, and aortas from both *Apoe*$^{-/-}$ and WT mice were pinned up on a thin foam pad and placed on an imaging plate (BAS-IP-2025 and −2040 SR storage phosphor screens, GE Healthcare Life Sciences, Pittsburgh, PA, USA). After an exposure period (3–5 days, depending on the experimental setup), the imaging plates were read at a pixel resolution of 50 µm with an Amersham Typhoon FLA 9500 Phosphor Imager (GE Healthcare Life Sciences). ImageQuant TL 8.2 software (GE Healthcare Life Sciences) was used for quantitative analysis of ^{89}Zr-tracer uptake in the aorta. ROIs were manually drawn on each aorta, including whole aorta (WA), aortic arch, thoracic aorta (TA), and abdominal aorta (AA). The plaque ROIs were outlined in the aortic arch, guided by a corresponding image of full-length aorta stained with Sudan IV. Negative control ROIs were determined for both thoracic and abdominal parts of aortas as a nonplaque area within the aorta with the lowest activity. The background counts for the ROIs were outlined on each imaging plate. The threshold intensity values were set by estimating the lowest (lightest) pixel within the corresponding section image. The ^{89}Zr radioactivity uptake in each ROI was calculated as the total intensity, photostimulated luminescence (PSL) per ROI area (mm^2), corrected for the radioactive decay between injection and PI reading time points, normalized for differences in injected dose per gram of mouse weight and then background subtracted. To compare different image acquisitions, the ratios were calculated between the signals from the whole aorta of each animal and the whole aorta of the WT animal showing the lowest signal

on each plate. Additionally, the ratios between the plaque areas in the aortic arch and nonplaque areas averaged over the whole aorta of each animal were calculated to evaluate plaque specificity.

Semiautomatic Calculation of Radiotracer Accumulation in Plaque from PI-ARG

To improve the reproducibility of estimating radiotracer accumulation in atherosclerotic lesions as registered on PI, a semiautomatic routine was developed in MATLAB R2015b (MathWorks, Natick, MA, USA). Images obtained from the scanning of storage phosphor plates exported in TIF format with data scaled to the maximum intensity in the respective plate lost any absolute value. Consequently, each sample was processed independently. For each aorta, a fixed-size rectangular ROI was centered over the aorta. A local background was then calculated from the mean of ±20 pixels on the perimeter of this ROI and subtracted from the aortic image data (I-bkg). I-bkg was smoothed, and the edge of the aorta was determined on this image using a threshold of 0.5 × mean I-bkg intensity. A mask was generated using this edge and applied to I-bkg to simplify subsequent calculations because the processed image then only contained data within the aortic border. For each processed image, a small rectangular ROI was positioned manually over a region of the aorta considered to be normal, and the mean intensity (mns) of the rectangular ROI was calculated. The plaque area was considered to consist of pixels with intensity values > mns × 2. The plaque burden was expressed as the plaque area pixels divided by all pixels in the aortic region, hence corresponding to the plaque burden as detected by the radiotracer.

Statistical Analyses

Data are represented as mean ± SEM if not stated otherwise. Statistical analyses were conducted in GraphPad Prism (version 7 for Macintosh). Statistical differences between the two group means were determined using a Student *t* test. To compare more than two groups, a one-way ANOVA was applied with a Tukey post hoc test. $P<0.05$ was regarded as significant in tests of statistical inference.

Results

Radiotracer Characteristics

The probe quality has previously been characterized in our group by MALDI-TOF MS.[25] The radiochemical yield was 95% (based on HPLC analysis of the crude product). To determine the uptake of the FITC-labeled probes by circulating blood cells, whole blood was analyzed using flow cytometry after 5 min of probe administration, and less than 0.25% of the circulating leukocytes took up the FITC-labeled probes.

To visualize and quantify the accumulation of ^{89}Zr-Mal-HSA in the aortic arch we used in vivo PET TRCs obtained from 1 h dynamic scans and illustrated as SUV_{max} in the aortic arch, SUV_{mean} of blood pool, and TBR_{max} (Figure 2). The blood kinetic curves for pure ^{89}Zr radioisotope showed a higher blood activity and slower clearance compared with ^{89}Zr-HSA and ^{89}Zr-Mal-HSA alone. In turn, ^{89}Zr-HSA showed a much slower blood clearance than ^{89}Zr-Mal-HSA (Supplementary Figure S1).

To determine their suitability as a vascular diagnostic imaging tool with regard to background signal, the TBR_{max} ± SEM for the activities from the aortic arch (SUV_{max}) and from the blood pool (SUV_{mean}) were calculated from the 1 h dynamic scans, and the values averaged over the last 15 min of the scan. TBRs for ^{89}Zr-Mal-HSA and ^{89}Zr-HSA for mice aged 16 and 20 weeks are summarized in Table 1 (in vivo). While evaluating TBRs, we found a significant ($P<0.05$) 41% increase in uptake of ^{89}Zr-Mal-HSA vs ^{89}Zr-HSA in *Apoe*$^{-/-}$ mice aged 16 weeks. No significant differences were observed when comparing TBRs in *Apoe*$^{-/-}$ and WT mice injected with ^{89}Zr-Mal-HSA or ^{89}Zr-HSA.

Animal Lipid Profiles and Plaque Burden

Mouse characteristics such as plasma lipid levels, blood glucose, and lesion percentage were measured and are summarized in Supplementary Table S1. HDL and VLDL/LDL levels differed significantly between WT and *Apoe*$^{-/-}$ mice ($P<0.0001$ and $P<0.0001$, respectively). No significant differences were seen for TG, NEFAs, or blood glucose levels between WT and *Apoe*$^{-/-}$ mice. Weight did not differ significantly between mice at 16 or 20 weeks of age. Plaque burden did not differ significantly between *Apoe*$^{-/-}$ mouse groups (Mal-HSA vs HSA); however, the differences were significant when comparing plaque burden within different parts of the aorta within each *Apoe*$^{-/-}$ mouse group: arch vs TA ($P<0.0001$) and arch vs abdominal aorta ($P<0.0001$) (Supplementary Table S1).

^{89}Zr-Mal-HSA Accumulated in the Atherosclerotic Aortic Arch of *Apoe*$^{-/-}$ Mice

To evaluate the in vivo applicability for quantitative imaging and targeting of atherosclerotic aortas, the activity in

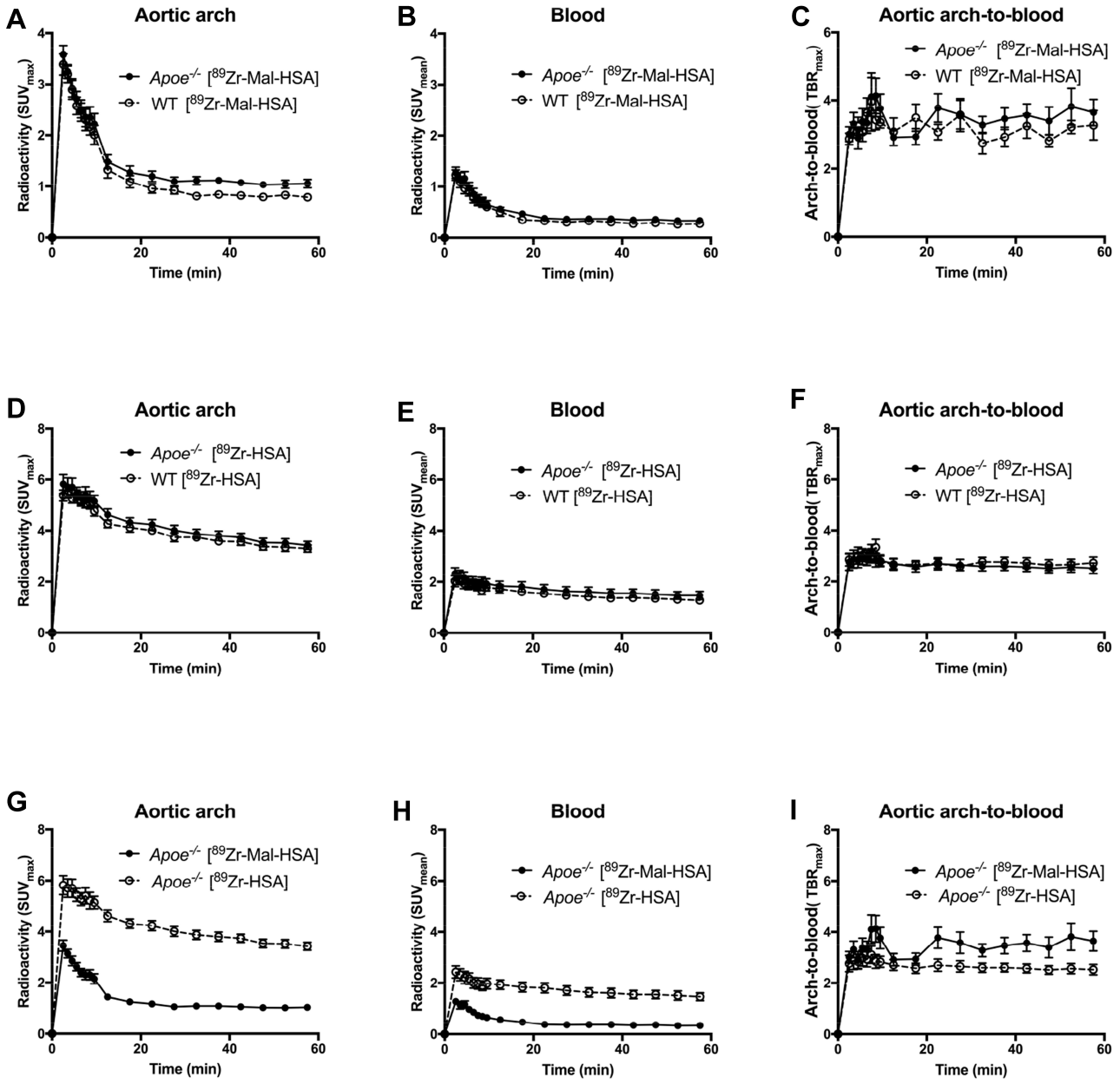

Figure 2 In vivo PET time radioactivity curves from aortic arch, blood and aortic arch-to-blood ratio in mice injected with (**A**–**C**) ^{89}Zr-Mal-HSA, (**D**–**F**) ^{89}Zr-HSA, or (**G**–**I**) ^{89}Zr-Mal-HSA vs ^{89}Zr-HSA. Radiotracer measurements are presented as SUV_{max}, TBR_{max}, and mean ± SEM. HSA WT (n= 10), HSA *Apoe*$^{-/-}$ (n=10), Mal-HSA WT (n=11) and Mal-HSA *Apoe*$^{-/-}$ (n=12).

the aortic arch was measured by PET in vivo, and images were overlaid with MR images for anatomical information (Figure 3A). Already at 16 weeks of age, *Apoe*$^{-/-}$ mice injected with ^{89}Zr-Mal-HSA showed a 26% (P<0.05) higher radiotracer uptake than WT mice, and *Apoe*$^{-/-}$ mice aged 20 weeks showed a 20% (P<0.05) higher uptake. The average activity from the aortic arch was measured 45–60 min p.i. from dynamic PET scans and is presented as SUV_{max} (Figure 3B).

We also sought to compare the activity in the aortic arch originating from intravenously injected ^{89}Zr-Mal-HSA radiotracer with the criterion standard radiotracer, ^{18}F-FDG, in the same animal. The comparison was facilitated by the short half-life of ^{18}F-FDG injected into the animals on day 1 and compared with ^{89}Zr-Mal-HSA radioactive uptake on day 2. ^{18}F-FDG showed higher SUV_{max} values overall in the PET within the same animal in vivo, but atherosclerotic and WT mice at 16 and 20 weeks of

Table 1 Target-to-Background Ratios (TBRs) Measured from in vivo PET Images and ex vivo Gamma Counter Measurements for the Different Radiotracers

	^{89}Zr-Mal-HSA		^{89}Zr-HSA		^{18}F-FDG	
In vivo	WT (n=11)	*Apoe*$^{-/-}$ (n=12)	WT (n=10)	*Apoe*$^{-/-}$ (n=10)		
16wTBR$_{Aorta:blood}$	2.99 ± 0.18	3.56 ± 0.40	2.67 ± 0.21	2.53 ± 0.19		
20wTBR$_{Aorta:blood}$	2.74 ± 0.26	3.33 ± 0.33	2.86 ± 0.21	2.65 ± 0.23		
Ex vivo		*Apoe*$^{-/-}$ (n=4)		*Apoe*$^{-/-}$ (n=3)		*Apoe*$^{-/-}$ (n=4)
20wTBR$_{Aorta:blood}$		5.35 ± 0.58		0.06 ± 0.01		7.43 ± 2.57
20wTBR$_{Aorta:heart}$		0.56 ± 0.05		0.35 ± 0.02		0.15 ± 0.07

Notes: Data are represented as mean ± SEM from 1 h dynamic PET scans in vivo and from biodistribution study 1 h p.i. Abbreviation 16 weeks of age (16w), 20 weeks of age (20w).

age showed no significant difference in radiotracer signals (Figure 3C).

Blocking Liver Uptake Increased Aortic Accumulation of ^{89}Zr-Mal-HSA

To investigate the radiotracer distribution and clearance from *Apoe*$^{-/-}$ mice, we studied the biodistribution of ^{89}Zr-Mal-HSA (Supplementary Figure S2A) and ^{89}Zr-HSA (Supplementary Figure S2B). ^{89}Zr-labeled Mal-HSA or HSA was injected into *Apoe*$^{-/-}$ mice that were fed a WD. The mice were euthanized at 1, 4, 24, and 48 h p.i. and the biodistribution was measured by gamma counting of radiotracer activity in each organ. Analysis of the biodistribution showed that both ^{89}Zr-Mal-HSA and ^{89}Zr-HSA accumulate in the liver, spleen, kidneys, iliac lymph nodes, and bone. Trivial to no accumulation was observed in the brain of mice injected with ^{89}Zr-Mal-HSA or ^{89}Zr-HSA. The blood kinetic profile showed high circulating levels of ^{89}Zr-HSA for at least 4 h p.i. while ^{89}Zr-Mal-HSA was almost completely cleared from the circulation after 1 h (Supplementary Figure S2). Target-to-background values (TBR ± SEM) were calculated for the aorta using either blood or heart activities as the background at 1 h p.i. for ^{89}Zr-Mal-HSA, ^{89}Zr-HSA, and for ^{18}F-FDG, and these are summarized in Table 1 (ex vivo). The TBRs for ^{89}Zr-Mal-HSA were higher than those for ^{89}Zr-HSA, but the measured activity from ^{89}Zr-HSA was higher than that from ^{89}Zr-Mal-HSA in the heart (2.2–2.7-fold) and in the aorta (1.6–3.3-fold). For ^{89}Zr-Mal-HSA in the aorta, the highest levels of activity observed were at 1 and 4 h p.i., after which the levels decreased, indicating peak uptake in the aorta around 1–4 h p.i. In the heart, the highest levels

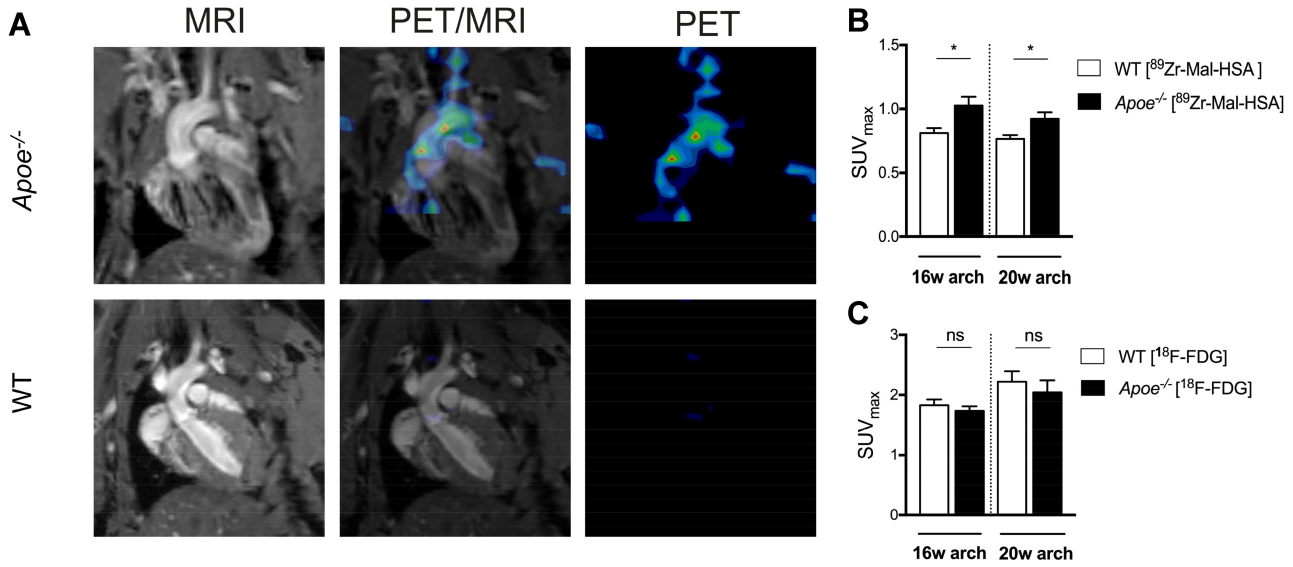

Figure 3 (**A**) Representative microPET/MR images showing accumulation of ^{89}Zr-Mal-HSA in the aortic arch of *Apoe*$^{-/-}$ mice compared with accumulation in wild-type (WT) mice at 20 weeks (1 h dynamic scan, 45 min p.i.). (**B**) The SUV$_{max}$ values for ^{89}Zr-Mal-HSA at 16 and 20 weeks were respectively 26% and 20% higher in *Apoe*$^{-/-}$ mice than in WT control mice. (**C**) No difference in SUV$_{max}$ was found in the aortic arch 40 min p.i. of ^{18}F-FDG in the same animals. Data are presented as mean ± SEM. Mal-HSA WT (n=11), Mal-HSA *Apoe*$^{-/-}$ (n=12), FDG WT (n=21) and FDG *Apoe*$^{-/-}$ (n=22). *P<0.05, ns = nonsignificant, as indicated.

were observed at 1 h p.i., indicating a 1.4-fold higher activity than that at 48 h p.i.; for the aorta, the highest levels were also observed at 1 h p.i. with a 1.6-fold higher activity than that at 48 h p.i. However, when comparing aorta-to-blood ratios, the highest TBRs for ^{89}Zr-Mal-HSA were observed 48 h p.i. (Supplementary Figure S3).

In an attempt to block or presaturate the off-target uptake by the liver and spleen, nonradiolabeled Mal-HSA (1 mg) was circulated for 15 min prior to injection of ^{89}Zr-Mal-HSA. This reduced the radiotracer accumulation in the liver by a factor of 2.1 and in the spleen by a factor of 2.2, as measured using a gamma counter. As expected, the blood activity increased considerably (195-fold) and interestingly the aortic activity increased 1.6-fold in *Apoe*$^{-/-}$ mice that received the precirculated nonradiolabeled probe, compared with mice that did not. However, no effect was observed for the heart (fold change 0.98).

Gamma Counter Measurement of ^{89}Zr-Mal-HSA Accumulation in Atherosclerotic Aortas Corroborated the in vivo PET Data

We compared the activity from the aorta in *Apoe*$^{-/-}$ (%ID/organ ± SEM; $8.6{\cdot}10^{-3}$ ± $0.63{\cdot}10^{-3}$) and WT ($6.5{\cdot}10^{-3}$ ± $0.25{\cdot}10^{-3}$) mice, as measured by gamma counter. A 32% (P<0.01) higher ^{89}Zr-Mal-HSA activity was observed in *Apoe*$^{-/-}$ mice 48 h p.i. in 20-week-old mice (Figure 4A). To compare the differences between ^{89}Zr-Mal-HSA and ^{89}Zr-HSA, the activity was divided by the activity measured from blood. Mice injected with ^{89}Zr-**Mal**-HSA had an approximately 8-fold higher aorta-to-blood ratio ($TBR_{Aorta:Blood}$ = 19.49 ± 3.74) than mice injected with the nonspecific ^{89}Zr-**HSA** probe ($TBR_{Aorta:Blood}$ = 2.48 ± 0.36) (Figure 4B).

PI-ARG of ^{89}Zr-Mal-HSA Showed Quantitative Accumulation in Atherosclerotic Plaques

To verify the accumulation of radiotracer in atherosclerotic lesions after circulation, whole aortas and the aortic root sections of *Apoe*$^{-/-}$ and WT mice were exposed on storage phosphor imager plates. The aortas and aortic root sections from *Apoe*$^{-/-}$ mice showed high atherosclerotic plaque signals compared with WT mice (Figures 5, 6, and 7). Quantitative ARG measurements (PSL/mm^2) showed a 34% significant (P<0.05) increase in radioactive uptake of ^{89}Zr-Mal-HSA in the whole aortas of *Apoe*$^{-/-}$ mice compared with the whole aortas of WT mice (Figure 5D).

Furthermore, we compared the signals of ^{89}Zr-Mal-HSA in the total plaque area in the aortic arch with nonplaque areas (three averaged ROIs over the whole aorta) for the *Apoe*$^{-/-}$ mice. TBR ± SEM was calculated as the signal obtained from the aortic arch plaques, divided by the signal from nonplaque areas used as a background for comparing the plaque specificity of ^{89}Zr-Mal-HSA and ^{89}Zr-HSA. The ARG measurements of TBR corroborated the PET measurements of TBR (Figure 2I), showing a significant (P<0.001) 44% increase for ^{89}Zr-Mal-HSA (2.94±0.18) over that for nonmodified ^{89}Zr-HSA (2.05±0.07), indicating a higher plaque specific uptake of ^{89}Zr-Mal-HSA (Figure 5E). We developed an alternative method to determine the specificity of the ^{89}Zr-Mal-HSA radiotracer that identifies the atherosclerotic plaque burden by applying semi-automatic calculations of the plaque signal in the whole aorta using MATLAB. The calculations showed an approximately 12-fold higher signal of ^{89}Zr-Mal-HSA in the plaque areas in the whole aortas of *Apoe*$^{-/-}$

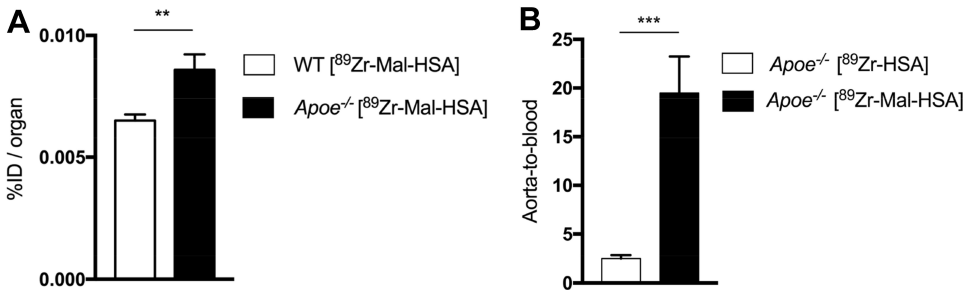

Figure 4 Gamma counter measurements of ^{89}Zr-labeled probe uptake in whole aortas (WA). (**A**) Results showing a significant 32% increase in activity (% injected dose (ID)/organ) in *Apoe*$^{-/-}$ mice compared with WT mice. (**B**) Results showing an approximate 8-fold increase in aorta-to-blood ratio ((%ID/g aorta)/(%ID/g blood)) 48 h p.i., comparing ^{89}Zr-Mal-HSA with nonspecific ^{89}Zr-HSA in WA of *Apoe*$^{-/-}$ mice. Data are presented as mean ± SEM. Mal-HSA WT (n=11), Mal-HSA *Apoe*$^{-/-}$ (n=12), and HSA *Apoe*$^{-/-}$ (n=10). **P<0.01 and ***P<0.001 as indicated.

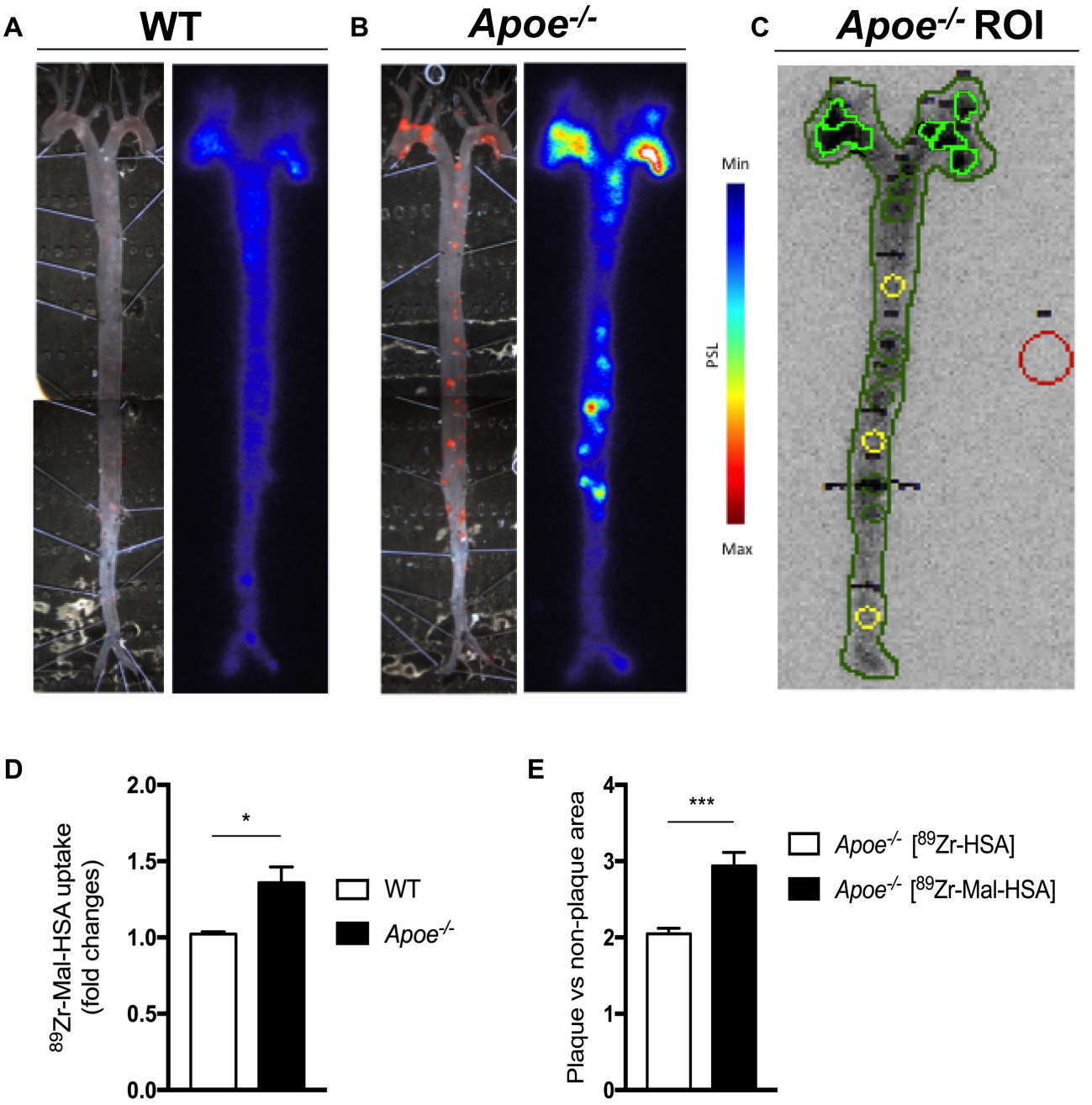

Figure 5 Autoradiography analysis of the ^{89}Zr-tracer uptake in mouse aortas. Representative PI-ARG image of (**A**) a control aorta from WT mouse compared with (**B**) *Apoe*$^{-/-}$ mouse, showing a detectable PI signal from plaque areas verified by Sudan IV staining of plaques (**A** and **B**, left panels respectively). (**C**) Illustrative example of quantitative analysis of gray-scale images in ImageQuant; ROIs (dark green) are placed to outline the whole aorta (WA) and in plaque regions in the thoracic and abdominal aorta, as well as in nonplaque regions (yellow). The highlighted green shows ROIs in the plaque area within the arch area, and the background ROI is shown in red. (**D**) Quantification of PI images of WA of WT and *Apoe*$^{-/-}$ mice 48 h p.i. of ^{89}Zr-Mal-HSA. Data are presented as fold changes between radiotracer signals from the WA compared with the WA of the control animal. (**E**) Quantification of PI images of aortas in *Apoe*$^{-/-}$ mice 48 h p.i. of ^{89}Zr-Mal-HSA or ^{89}Zr-HSA. Data in (**E**) are presented as the ratio of mean intensity signals (PSL/mm^2) from aortic arch plaque areas and nonplaque areas within each animal. All data are presented as mean ± SEM. Mal-HSA WT (n=5), Mal-HSA *Apoe*$^{-/-}$ (n=11), and HSA *Apoe*$^{-/-}$ (n=9). *P<0.05 and ***P<0.001 as indicated.

mice (9.4±1.4%) compared with control mice (0.8 ±0.3%, P<0.0001; Figure 6C): these values corresponded well to the plaque area coverage calculated as a percentage of the whole aorta (7.6±3.8%) as identified by Sudan IV staining (Supplementary Table S1).

Presence of Macrophages in ^{89}Zr-Mal-HSA-Positive Aortic Root Sections

To verify the macrophage content in atherosclerotic plaques with a ^{89}Zr-Mal-HSA activity, we stained aortic root sections immunohistochemically. The presence of

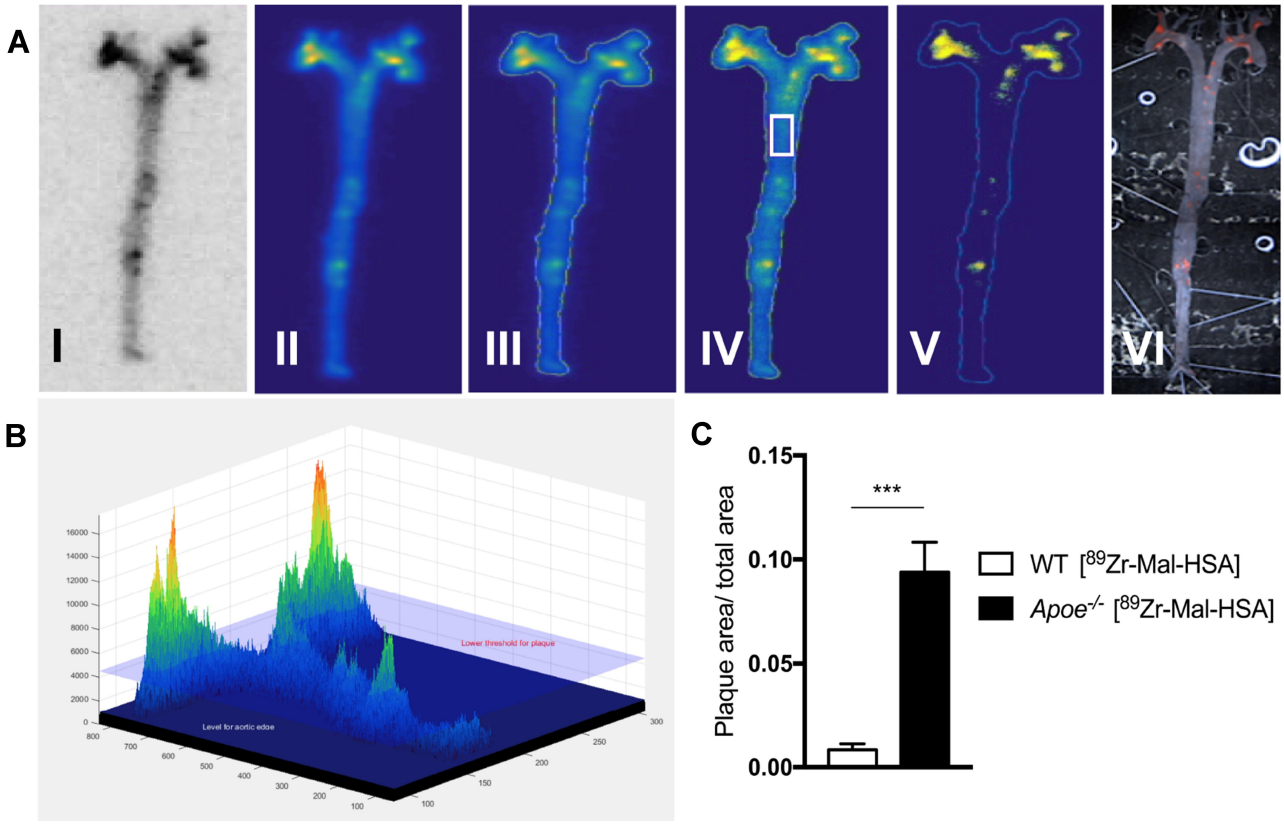

Figure 6 Semiautomatic calculation of plaque signals from PI-ARG. (**A**) Illustrations of aortas from *Apoe*$^{-/-}$ mice, showing the step-by-step calculations (I–V) in MATLAB. The white box outlines the nonplaque area used to set a threshold. The remaining significant plaques above the threshold are illustrated in (V). Sudan IV staining (VI) of plaque burden corresponded well to the plaque signal identified by ^{89}Zr-Mal-HSA. (**B**) 3D intensity plot illustrating the threshold level (blue slice). (**C**) Semiautomated measurements from (**A**) and (**B**) were used to calculate further the number of pixels, with significant intensities divided by the total number of pixels in the aorta. The plaque signal of ^{89}Zr-Mal-HSA differed significantly when comparing *Apoe*$^{-/-}$ (n=8) and WT (n=6) mice. Data are presented as mean ± SEM. ***P<0.001 as indicated.

macrophages in aortic root sections in *Apoe*$^{-/-}$ mice was verified by anti-CD68 staining and overlapped with scavenger receptor A staining by anti-SR-A1. Aortic root sections from WT mice lacked a ^{89}Zr-Mal-HSA activity and were also negative for CD68 and SR-A1. In both *Apoe*$^{-/-}$ and WT mice smooth muscle alpha-actin (SMA) positive staining was found in the media, and von Willebrand Factor (vWF) stainings were positive on endothelial cells lining vessels or covering both sides of aortic valve leaflets. We found that the expression of classic vSMC and endothelial cell markers was low in the cap area of the atherosclerotic plaques in *Apoe*$^{-/-}$ mice and did not substantially overlap with the SR-A1 staining in our *Apoe*$^{-/-}$ animal model (Figure 7). The negative controls for the immunohistochemistry are shown in Supplementary Figure S4.

Discussion

Based on our previous findings that ^{89}Zr-Mal-HSA specifically binds to SR-A1 receptor on macrophages in vitro,[25] we hypothesized that its target specificity and affinity were sufficiently high to be used for specific targeting of inflamed atherosclerotic lesions in vivo.

Our tracer was cleared from the blood circulation rapidly; hence, we expected low levels of interfering noise for use in vascular imaging. Other beneficial advantages of HSA-based probes are their low toxicity profile[18] and stability in vivo by radiolabeling with DFO.[32]

We found uptake of ^{89}Zr-Mal-HSA in atherosclerotic aortas, shown in vivo by qualitative and quantitative PET imaging, and corroborated by ex vivo gamma counting and PI-ARG measurements. We confirmed a high plaque specificity of ^{89}Zr-Mal-HSA with PI-ARG measurements using two different methods for quantification. In the manual method, the difference between Mal-HSA and HSA for distinguishing plaque vs nonplaque areas in the same mouse was calculated and the superiority of ^{89}Zr-Mal-HSA over the nontargeted ^{89}Zr-HSA was demonstrated. When using the semiautomated method, the ^{89}Zr-Mal-HSA signal coming only from plaque areas in the same aorta could be

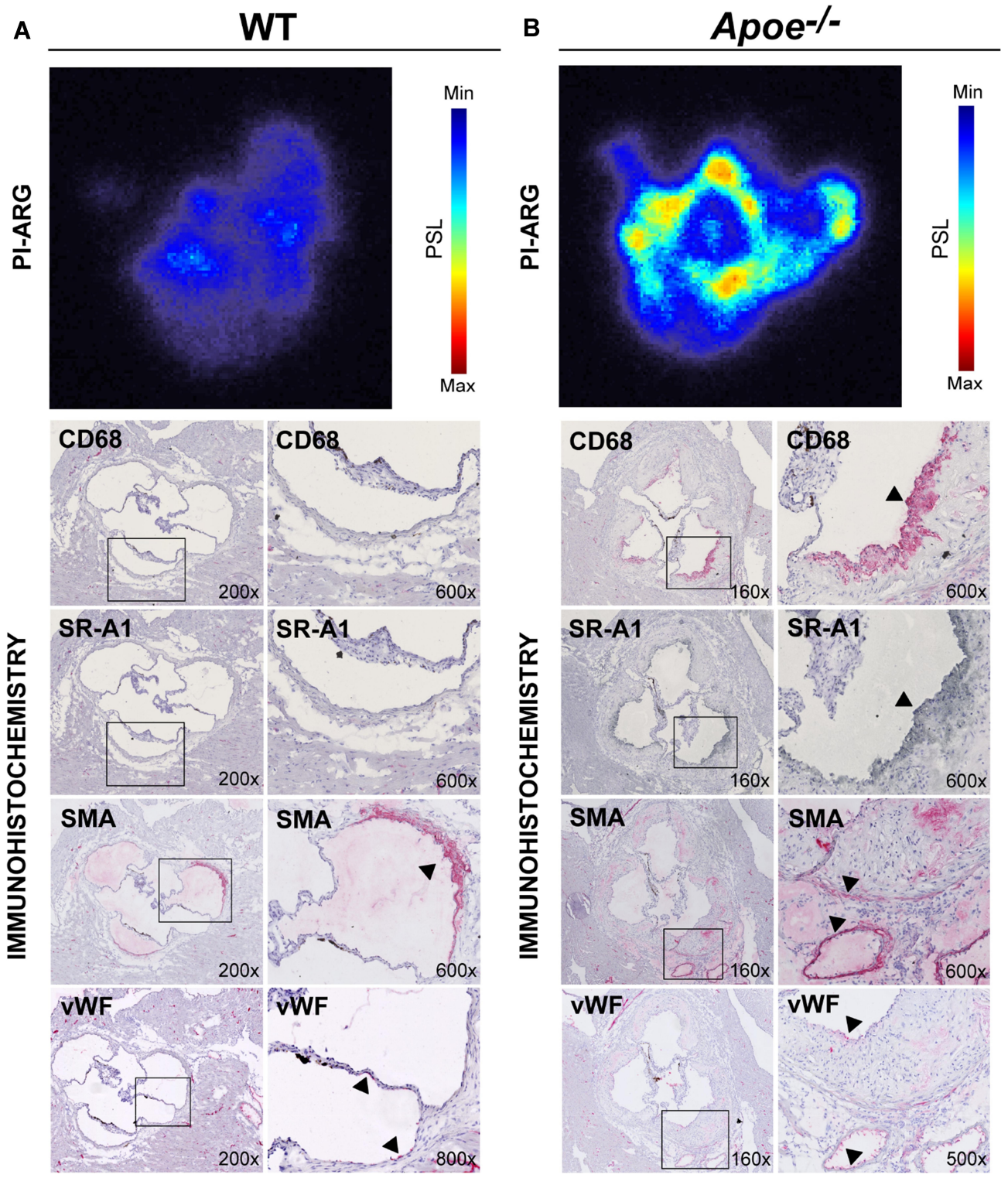

Figure 7 Representative aortic root sections from (**A**) WT mouse and (**B**), *Apoe*$^{-/-}$ mouse including zoomed areas. Upper panel showing ^{89}Zr-Mal-HSA signal in macrophage-rich plaque areas in aortic root sections from an *Apoe*$^{-/-}$ mouse, measured by PI-ARG. Lower panels showing adjacent sections stained for macrophages with anti-mouse CD68 (red), for scavenger receptor A1 with anti-mouse SR-A1 (red WT, black *Apoe*$^{-/-}$), for vascular smooth muscle cells with anti-mouse smooth muscle alpha-actin (SMA) (red), and for endothelial cells with anti-mouse von Willebrand Factor (vWF) (red), indicated by the black arrowheads.

distinguished by setting a cutoff threshold to define the plaque signal. Thus, both methods verified the specificity of ^{89}Zr-Mal-HSA for plaques. However, overall radioactivity measured using a gamma counter was higher from ^{89}Zr-HSA than from ^{89}Zr-Mal-HSA, in both the heart (2.2–2.7-fold) and in the whole aorta (1.6–3.3-fold). This is possibly due to

longer blood circulation time for ^{89}Zr-HSA that in turn might give rise to an unspecific vascular wall activity through interstitial leakage.

A significant difference in radioactive signal was measured by PET imaging in the aortic arch of *Apoe*$^{-/-}$ mice, as early as 16 weeks old and fed a WD for 8 weeks, compared with control animals, indicating utility in early diagnostic imaging of atherosclerosis. Nakashima et al reported monocyte adhesion and the development of foam cell lesions in the aortas of *Apoe*$^{-/-}$ mice fed a WD for 8–10 weeks and the formation of intermediate lesions beginning from 10 weeks on a WD.[33] After 15 weeks of a WD, the same study found the development of increasingly fibrotic plaques. This would appear to indicate that 8–12 weeks of a WD is a suitable time for targeting inflammatory markers in experimental atherosclerotic plaques in *Apoe*$^{-/-}$ mice. Other studies using older mice with greater disease, or larger animal models, showed a 25–100% increase in the aortic uptake of various preclinical radiotracers ex vivo or in vivo.[11,20,34] In a study by Davies et al, a significant uptake of ^{18}F-FDG differences in aorta in 9-month-old atherosclerotic rabbits was shown by ex vivo gamma counting and PET imaging, whereas no significant difference could be found by PET imaging in vivo.[35] This research field has been hampered by difficulties encountered in PET imaging of small animals in vivo. Using our broad approach with multiple methodologies, we have—to some extent—successfully bypassed these difficulties.

SR-A1 is a widely studied key receptor in atherogenesis and is expressed mainly by macrophages, monocytes and foam cells in atherosclerotic plaques, but could also be expressed by endothelial cells and vSMCs during oxidative stress.[36] We found that SR-A1 staining co-localizes with CD68 expressing cells. When comparing immunohistochemistry results with PI-ARG analysis, cells expressing SMA and vWF do not seem to primarily take up our radiotracer as indicated by a very low ARG signal in WT mice. SR-A1 could also be found on mature macrophages in the liver sinusoid, such as Kupffer cells and on sinusoidal endothelial cells, as well as on alveolar and splenic macrophages, and on postcapillary venules in the lymph nodes.[37,38] A high activity is expected in the reticuloendothelial system, where most of the scavenger receptor-expressing cells reside,[39] indeed, the highest activities from ^{89}Zr-Mal-HSA accumulation were observed in the liver and spleen, which could possibly impair radiotracer concentrations at target sites. By partial saturation of the uptake capacity in the liver and spleen by the administration of non-radiolabeled probe (Mal-HSA) 15 min prior to injection of ^{89}Zr-Mal-HSA, an increased aortic activity, as measured by gamma counting and PI-ARG, was calculated.

We consider ^{89}Zr-Mal-HSA targeting SR-A1 on macrophages to be more specific than the currently utilized ^{18}F-FDG for macrophage targeting in early atherosclerotic lesions. Studies utilizing ^{18}F-FDG have shown small nonsignificant differences in uptake between WD-fed (8 weeks) and chow diet-fed *Apoe*$^{-/-}$ mice, as measured by microPET 180 min p.i. However, larger and significant differences with increasing time on a WD were shown.[40] Another study found that a high brown adipose tissue uptake of ^{18}F-FDG, especially when given to awake animals, constitutes a major confounding factor in the imaging of atherosclerosis in *Apoe*$^{-/-}$ mice.[41] A high prescan glucose level may constitute another confounding factor, which may also be important for our study, and was previously reported in humans.[42] In our relatively early disease model of atherosclerosis, no differences were observed when comparing the ^{18}F-FDG PET signal in the aortic arch of *Apoe*$^{-/-}$ mice with control mice at the chosen imaging time of 40–90 min p.i. This indicates an advantage for Mal-HSA as an early diagnostic molecular imaging probe for targeting inflammation in atherosclerotic lesions. Rudd et al suggest that, apart from the early stages of atherosclerosis, a potential reason for this could be the chosen time point; an optimal time point would instead be 90–180 min p.i.[43,44] Additionally, Blomberg et al show that TBR quantification was improved at 180 min as opposed to 90 min p.i.[45]

^{89}Zr has been applied in many imaging applications including humans,[32,46–51] and its inherited characteristics with a long half-life of 78.4 h allow for repeated and longitudinal studies of metabolic or molecular changes. Since, in the current study, we could show aortic accumulation within 1 h, as demonstrated by PET and verified by gamma counter measurements ex vivo with a possible peak around 4 h, one might argue that it could be possible to use an isotope with a shorter half-life. However, the TBRs (aorta-to-blood) from biodistribution data showed an increasing trend over time, with a peak at the 48 h, supporting imaging with radioisotopes with longer half-life when imaging atherosclerotic plaques to optimize the image contrast. ^{89}Zr has a lower e^+ energy than, for example, ^{68}Ga, and is comparable with ^{18}F or ^{64}Cu in this sense, which makes the radiotracer attractive for imaging applications of smaller structures. Interestingly, our probe design makes it possible to couple various radio- or paramagnetic metals for specific areas of use. PET/MRI also offers lower radiation exposure compared to coregistration with CT. Combining conventional anatomical imaging with noninvasive imaging that incorporates molecular information about the disease burden, plaque composition, and

metabolic activity would help predict cardiovascular risk, direct therapeutic interventions and improve patient management.

Limitations

In the present study, we used a separate 9.4 T MR-scanner with a favorable high spatial resolution for structural positioning and applied fusion software. PET/MRI offers lower radiation exposure compared to coregistration with CT. However, the nonsimultaneous imaging of PET and MRI is a limitation when it comes to partial volume effects. In addition, cardiac and respiratory motions, although gated for, will still impact quantification negatively in small structures such as the atherosclerotic plaques in mice.[44,52] The liver might be the dose-limiting organ for this particular radiotracer, as evidenced in other human dosimetry studies on immuno-PET tracers in the field of oncology.[53,54] Human radiation dosimetry studies as well as improvements in imaging acquisition, coregistration, and off-target activity reduction, would be desirable to overcome barriers for clinical translation.

Conclusion

^{89}Zr-Mal-HSA appears to be a feasible radiotracer in experimental PET imaging, and it allowed for extensive ex vivo evaluation that identified inflamed plaques, even at relatively early stages of atherosclerosis. Its blood kinetic profile may be advantageous for vascular imaging, provided that the initial concentration is sufficient for a relevant uptake, which seems to be the case. Our study provides a scientific foundation for the development of new diagnostic tools that target macrophage-rich areas of inflammation in atherosclerosis.

Ethics Statement

Institutional and national guidelines for the care and use of laboratory animals were followed, and all animal experiments were approved by the Stockholm Animal Ethics Committee.

Acknowledgments

We thank the following experts at Karolinska Institutet, Stockholm, Sweden: Nancy Simon for histological sectioning of aortic roots, Mariette Lengquist for immunohistochemistry-staining protocols, Annelie Falkevall and Sofia Wittgren for technical assistance with the cholesterol analyses. We are also grateful to Joe Hirano at GE Healthcare, Uppsala, Sweden for valuable comments on the quantification of autoradiography.

Author Contributions

All authors contributed toward data analysis, drafting and revising the paper, gave final approval of the version to be published and agree to be accountable for all aspects of the work.

Funding

The study was supported by the Swedish Research Council (22036); the Swedish Heart Lung Foundation (20150423, 20170669); the Swedish state under the agreement between the Swedish government and the county councils, the ALF-agreement (20150517, 447561, 726481, 824851); and the Söderberg Foundations and Karolinska Institutet.

Disclosure

The authors declare that they have no conflicts of interest in this work.

References

1. Geovanini GR, Libby P. Atherosclerosis and inflammation: overview and updates. *Clin Sci (Lond)*. 2018;132(12):1243–1252. doi:10.1042/CS20180306
2. Tarkin JM, Dweck MR, Evans NR, et al. Imaging Atherosclerosis. *Circ Res*. 2016;118(4):750–769. doi:10.1161/CIRCRESAHA.115.306247
3. Libby P. Inflammation in atherosclerosis. *Arterioscler Thromb Vasc Biol*. 2012;32(9):2045–2051. doi:10.1161/ATVBAHA.108.179705
4. Bentzon JF, Otsuka F, Virmani R, Falk E. Mechanisms of plaque formation and rupture. *Circ Res*. 2014;114(12):1852–1866. doi:10.1161/CIRCRESAHA.114.302721
5. Goel S, Miller A, Agarwal C, et al. Imaging modalities to identity inflammation in an atherosclerotic plaque. *Radiol Res Pract*. 2015;2015:410967.
6. Kaufmann BA, Carr CL, Belcik JT, et al. Molecular imaging of the initial inflammatory response in atherosclerosis: implications for early detection of disease. *Arterioscler Thromb Vasc Biol*. 2010;30(1):54–59. doi:10.1161/ATVBAHA.109.196386
7. Kaufmann BA, Sanders JM, Davis C, et al. Molecular imaging of inflammation in atherosclerosis with targeted ultrasound detection of vascular cell adhesion molecule-1. *Circulation*. 2007;116(3):276–284. doi:10.1161/CIRCULATIONAHA.106.684738
8. Steinl DC, Kaufmann BA. Ultrasound imaging for risk assessment in atherosclerosis. *Int J Mol Sci*. 2015;16(5):9749–9769. doi:10.3390/ijms16059749
9. Phinikaridou A, Andia ME, Lavin B, Smith A, Saha P, Botnar RM. Increased vascular permeability measured with an albumin-binding magnetic resonance contrast agent is a surrogate marker of rupture-prone atherosclerotic plaque. *Circ Cardiovasc Imaging*. 2016;9:12.
10. Tang TY, Howarth SP, Miller SR, et al. The ATHEROMA (atorvastatin therapy: effects on reduction of macrophage activity) study. Evaluation using ultrasmall superparamagnetic iron oxide-enhanced magnetic resonance imaging in carotid disease. *J Am Coll Cardiol*. 2009;53(22):2039–2050. doi:10.1016/j.jacc.2009.03.018
11. Nahrendorf M, Zhang H, Hembrador S, et al. Nanoparticle PET-CT imaging of macrophages in inflammatory atherosclerosis. *Circulation*. 2008;117(3):379–387. doi:10.1161/CIRCULATIONAHA.107.741181

12. Tarkin JM, Joshi FR, Rudd JH. PET imaging of inflammation in atherosclerosis. *Nat Rev Cardiol*. 2014;11(8):443–457. doi:10.1038/nrcardio.2014.80
13. Ripa RS, Pedersen SF, Kjaer A. PET/MR Imaging in Vascular Disease: atherosclerosis and Inflammation. *PET Clin*. 2016;11(4):479–488. doi:10.1016/j.cpet.2016.05.009
14. Rudd JH, Narula J, Strauss HW, et al. Imaging atherosclerotic plaque inflammation by fluorodeoxyglucose with positron emission tomography: ready for prime time? *J Am Coll Cardiol*. 2010;55(23):2527–2535. doi:10.1016/j.jacc.2009.12.061
15. Hellberg S, Sippola S, Liljenback H, et al. Effects of atorvastatin and diet interventions on atherosclerotic plaque inflammation and [(18)F]FDG uptake in Ldlr(-/-)Apob(100/100) mice. *Atherosclerosis*. 2017;263:369–376. doi:10.1016/j.atherosclerosis.2017.04.004
16. Jarrett BR, Correa C, Ma KL, Louie AY. In vivo mapping of vascular inflammation using multimodal imaging. *PLoS One*. 2010;5(10):e13254. doi:10.1371/journal.pone.0013254
17. Joshi NV, Vesey AT, Williams MC, et al. 18F-fluoride positron emission tomography for identification of ruptured and high-risk coronary atherosclerotic plaques: a prospective clinical trial. *Lancet*. 2014;383(9918):705–713. doi:10.1016/S0140-6736(13)61754-7
18. Cao W, Lu X, Cheng Z. The advancement of human serum albumin-based molecular probes for molecular imaging. *Curr Pharm Des*. 2015;21(14):1908–1915. doi:10.2174/1381612821666150302120517
19. Hellberg S, Liljenback H, Eskola O, et al. Positron emission tomography imaging of macrophages in atherosclerosis with F-18-GE-180, a Radiotracer for Translocator Protein (TSPO). *Contrast Media Mol Imaging*. 2018;11.
20. Kim EJ, Kim S, Seo HS, et al. Novel PET Imaging of Atherosclerosis with 68Ga-Labeled NOTA-Neomannosylated Human Serum Albumin. *J Nucl Med*. 2016;57(11):1792–1797. doi:10.2967/jnumed.116.172650
21. Lapi SE, Lewis JS, Dehdashti F. Evaluation of hypoxia with copper-labeled diacetyl-bis(N-methylthiosemicarbazone). *Semin Nucl Med*. 2015;45(2):177–185. doi:10.1053/j.semnuclmed.2014.10.003
22. Matter CM, Wyss MT, Meier P, et al. 18F-choline images murine atherosclerotic plaques ex vivo. *Arterioscler Thromb Vasc Biol*. 2006;26(3):584–589. doi:10.1161/01.ATV.0000200106.34016.18
23. Robson PM, Dweck MR, Trivieri MG, et al. Coronary Artery PET/MR imaging: feasibility, limitations, and solutions. *JACC Cardiovasc Imaging*. 2017;10(10Pt A):1103–1112. doi:10.1016/j.jcmg.2016.09.029
24. Tarkin JM, Joshi FR, Evans NR, et al. Detection of Atherosclerotic Inflammation by (68)Ga-DOTATATE PET Compared to [(18)F]FDG PET Imaging. *J Am Coll Cardiol*. 2017;69(14):1774–1791. doi:10.1016/j.jacc.2017.01.060
25. Ahmed M, Baumgartner R, Aldi S, et al. Human serum albumin-based probes for molecular targeting of macrophage scavenger receptors. *Int J Nanomedicine*. 2019;14:3723–3741. doi:10.2147/IJN.S197990
26. Linton MF, Fazio S. Class A scavenger receptors, macrophages, and atherosclerosis. *Curr Opin Lipidol*. 2001;12(5):489–495. doi:10.1097/00041433-200110000-00003
27. Nakata A, Nakagawa Y, Nishida M, et al. CD36, a novel receptor for oxidized low-density lipoproteins, is highly expressed on lipid-laden macrophages in human atherosclerotic aorta. *Arterioscler Thromb Vasc Biol*. 1999;19(5):1333–1339. doi:10.1161/01.ATV.19.5.1333
28. de Winther MP, van Dijk KW, Havekes LM, Hofker MH. Macrophage scavenger receptor class A: A multifunctional receptor in atherosclerosis. *Arterioscler Thromb Vasc Biol*. 2000;20(2):290–297. doi:10.1161/01.ATV.20.2.290
29. Gough PJ, Greaves DR, Suzuki H, et al. Analysis of macrophage scavenger receptor (SR-A) expression in human aortic atherosclerotic lesions. *Arterioscler Thromb Vasc Biol*. 1999;19(3):461–471. doi:10.1161/01.ATV.19.3.461
30. Robbins CS, Hilgendorf I, Weber GF, et al. Local proliferation dominates lesional macrophage accumulation in atherosclerosis. *Nat Med*. 2013;19(9):1166–1172. doi:10.1038/nm.3258
31. Samen E, Lu L, Mulder J, et al. Visualization of angiogenesis during cancer development in the polyoma middle T breast cancer model: molecular imaging with (R)- C-11 PAQ. *EJNMMI Res*. 2014;4:11. doi:10.1186/2191-219X-4-17
32. Dilworth JR, Pascu SI. The chemistry of PET imaging with zirconium-89. *Chem Soc Rev*. 2018;47(8):2554–2571. doi:10.1039/C7CS00014F
33. Nakashima Y, Plump AS, Raines EW, Breslow JL, Ross R. APOE-DEFICIENT MICE DEVELOP LESIONS OF ALL PHASES OF ATHEROSCLEROSIS THROUGHOUT THE ARTERIAL TREE. *Arterioscler Thrombosis*. 1994;14(1):133–140. doi:10.1161/01.ATV.14.1.133
34. Hellberg S, Silvola JMU, Kiugel M, et al. 18-kDa translocator protein ligand (18)F-FEMPA: biodistribution and uptake into atherosclerotic plaques in mice. *J Nucl Cardiol*. 2017;24(3):862–871. doi:10.1007/s12350-016-0527-y
35. Davies JR, Izquierdo-Garcia D, Rudd JHF, et al. FDG-PET can distinguish inflamed from non-inflamed plaque in an animal model of atherosclerosis. *Int J Cardiovasc Imaging*. 2010;26(1):41–48. doi:10.1007/s10554-009-9506-6
36. Mietus-Snyder M, Friera A, Glass CK, Pitas RE. Regulation of scavenger receptor expression in smooth muscle cells by protein kinase C: a role for oxidative stress. *Arterioscler Thromb Vasc Biol*. 1997;17(5):969–978. doi:10.1161/01.ATV.17.5.969
37. Bieghs V, Verheyen F, van Gorp PJ, et al. Internalization of modified lipids by CD36 and SR-A leads to hepatic inflammation and lysosomal cholesterol storage in Kupffer cells. *PLoS One*. 2012;7(3):e34378. doi:10.1371/journal.pone.0034378
38. Hughes DA, Fraser IP, Gordon S. Murine macrophage scavenger receptor: in vivo expression and function as receptor for macrophage adhesion in lymphoid and non-lymphoid organs. *Eur J Immunol*. 1995;25(2):466–473. doi:10.1002/eji.1830250224
39. Horiuchi S, Takata K, Maeda H, Morino Y. Scavenger function of sinusoidal liver-cells - acetylated low-density lipoprotein is endocytosed via a route distinct from formaldehyde-treated serum-albumIN. *J Biol Chem*. 1985;260(1):53–56.
40. Hag AMF, Pedersen SF, Christoffersen C, et al. F-18-FDG PET imaging of murine atherosclerosis: association with gene expression of key molecular markers. *PLoS One*. 2012;7(11):9. doi:10.1371/journal.pone.0050908
41. Toczek J, Broisat A, Perret P, et al. Periaortic brown adipose tissue as a major determinant of F-18 -fluorodeoxyglucose vascular uptake in atherosclerosis-prone, ApoE(-/-) Mice. *PLoS One*. 2014;9(7):9. doi:10.1371/journal.pone.0099441
42. Bucerius J, Mani V, Moncrieff C, et al. Optimizing 18F-FDG PET/CT imaging of vessel wall inflammation: the impact of 18F-FDG circulation time, injected dose, uptake parameters, and fasting blood glucose levels. *Eur J Nucl Med Mol Imaging*. 2014;41(2):369–383. doi:10.1007/s00259-013-2569-6
43. Joshi F, Rosenbaum D, Bordes S, Rudd JHF. Vascular imaging with positron emission tomography. *J Intern Med*. 2011;270(2):99–109. doi:10.1111/j.1365-2796.2011.02392.x
44. Rudd JHF, Fayad ZA, Machac J, et al. Imaging of vulnerable atherosclerotic plaques with FDG-microPET: noFDG accumulation' Atherosclerosis 2006. *Atherosclerosis*. 2007;192(2):453–454. doi:10.1016/j.atherosclerosis.2006.10.027
45. Blomberg BA, Thomassen A, Takx RA, et al. Delayed (1)(8)F-fluorodeoxyglucose PET/CT imaging improves quantitation of atherosclerotic plaque inflammation: results from the CAMONA study. *J Nucl Cardiol*. 2014;21(3):588–597. doi:10.1007/s12350-014-9884-6

46. Fairclough M, Prenant C, Ellis B, et al. A new technique for the radiolabelling of mixed leukocytes with zirconium-89 for inflammation imaging with positron emission tomography. *J Labelled Comp Radiopharm*. 2016;59(7):270–276. doi:10.1002/jlcr.3392
47. Fischer G, Seibold U, Schirrmacher R, Wangler B, Wangler C. (89)Zr, a radiometal nuclide with high potential for molecular imaging with PET: chemistry, applications and remaining challenges. *Molecules*. 2013;18(6):6469–6490. doi:10.3390/molecules18066469
48. Majmudar MD, Yoo J, Keliher EJ, et al. Polymeric Nanoparticle PET/MR imaging allows macrophage detection in atherosclerotic plaques. *Circ Res*. 2013;112(5):755–761. doi:10.1161/CIRCRESAHA.111.300576
49. Senders ML, Que XC, Cho YS, et al. PET/MR imaging of malondialdehyde-acetaldehyde epitopes with a human antibody detects clinically relevant atherothrombosis. *J Am Coll Cardiol*. 2018;71(3):321–335. doi:10.1016/j.jacc.2017.11.036
50. Zeglis BM, Lewis JS. The bioconjugation and radiosynthesis of 89Zr-DFO-labeled antibodies. *J Vis Exp*. 2015;96.
51. Zhang Y, Hong H, Cai W. PET tracers based on Zirconium-89. *Curr Radiopharm*. 2011;4(2):131–139. doi:10.2174/1874471011104020131
52. Perrone-Filardi P, Dellegrottaglie S, Rudd JH, et al. Molecular imaging of atherosclerosis in translational medicine. *Eur J Nucl Med Mol Imaging*. 2011;38(5):969–975. doi:10.1007/s00259-010-1697-5
53. Laforest R, Lapi SE, Oyama R, et al. [(89)Zr]trastuzumab: evaluation of radiation dosimetry, safety, and optimal imaging parameters in women with HER2-positive breast cancer. *Mol Imaging Biol*. 2016;18(6):952–959. doi:10.1007/s11307-016-0951-z
54. Lindenberg L, Adler S, Turkbey IB, et al. Dosimetry and first human experience with (89)Zr-panitumumab. *Am J Nucl Med Mol Imaging*. 2017;7(4):195–203.